ChemComm

COMMUNICATION

View Article Online
View Journal | View Issue



Cite this: *Chem. Commun.*, 2025, **61**, 14931

Received 1st July 2025,
Accepted 20th August 2025

DOI: 10.1039/d5cc03658e

rsc.li/chemcomm

# A CRISPR Cas protein coronated AuNP nanostructure for enhanced uptake efficiency into cells

Zhaojia Deng,†[ac] Rui Sha,†[a] Hua Qin,[ab] Yingxu Shang,[ac] Aijiao Yuan,[ac] Wenjing Xie[ac] and Hanyong Peng *[ac]

**The effectiveness of nanotechnologies is often limited by their non-specific aggregation in biological environments. We developed a protein coronated nanostructure by functionalizing AuNPs with nucleic acid scaffolds and CRISPR Cas proteins, significantly enhancing nanoparticle stability and cellular uptake efficiency, making it a promising tool for imaging and biomedical applications.**

Nanoparticle-based technologies, such as AuNPs, have emerged as versatile tools in biomedicine owing to their facile synthesis, range of sizes, biological inertness, and unique optical properties.[1] These properties make them promising candidates for various biomedical applications, such as drug delivery, photothermal therapy, photodynamic therapy, and bioimaging. However, the effectiveness of nanoparticles is often hindered by their tendency to aggregate in complex biological environments, compromising their stability and functionality.[2,3] The stability and bioavailability of nanoparticles in biological media is crucial for retaining their properties and fully utilizing their biomedical potential.

The large specific surface area and high surface activity of nanoparticles can lead to aggregation, reducing their cellular delivery efficiency and increasing cytotoxicity, thus limiting their functionality in biological environments. Electrostatic repulsion is commonly employed to prevent the aggregation of nanoparticles. For instance, AuNPs prepared from citrate-reduced $HAuCl_4$ possess a diffusion double layer that generates repulsive forces among the particles at low ionic concentrations, with citrate acting as both a reducing agent and a stabilizer.[4] However, stabilization *via* electrostatic repulsion,[5] as seen in citrate/cetyltrimethylammonium bromide (CTAB)-modified AuNPs, is susceptible to pH, salt concentration, and metal ions in solution, posing challenges for biological applications.[6] Another approach involves modifying nanoparticles with polymers like poly(ethylene glycol) (PEG) to prevent particle agglomeration.[7,8] While this method can enhance stability, it may increase immunogenic activity and potentially cause acute injuries to organs.[9,10]

Furthermore, the introduction of nanoparticles into biological fluids results in the adsorption of proteins and small molecules onto their surface, forming unpredictable and nonspecific protein coronas. These coronas can mask the original functions of nanoparticles and alter their biological fate.[11,12] The dynamic and competitive nature of protein coronas in biological fluids makes their formation unpredictable and uncontrolled, diminishing the efficacy of nanoparticles in biomedical applications.[13,14]

To address these challenges,[15,16] an artificial protein corona nanostructure (PCN) has been developed to enhance intracellular delivery of AuNPs (Scheme 1). This study used thiol-modified DNA strands complementary to a DNA linker, capable of hybridizing with single-guide RNA (sgRNA), to functionalize the AuNPs, followed by the binding of a clustered regularly interspaced short palindromic repeats (CRISPR) associated protein (Cas9) to sgRNA to form a controlled protein corona nanostructure on the nanoparticle surface.[17] The study assessed the stability of these PCNs under diverse biological conditions, while also studying their uptake efficiency and mechanisms. The biocompatible PCN-based delivery platform not only mitigates non-specific aggregation but also enhances cellular uptake efficiency, positioning it as a promising strategy for imaging and biomedical applications.

To synthesize the self-assembled protein coronated nanostructure (PCN), the initial step involved modifying the surface of gold nanoparticles with a nucleic acid inner layer. This process entailed connecting the sgRNA to a thiol-modified anchor strand *via* a linker strand, resulting in the formation of a three-strand complex. By anchoring this nucleic acid complex to the surface of 20 nm gold nanoparticles through Au–S bonds facilitated by the thiol group at the 5′ end of the anchor strand, a nucleic acid inner layer was established, leading to the creation of a spherical nucleic acid (SNA) structure. The orientation of the nucleic acid scaffolds played a

[a] *State Key Laboratory of Environmental Chemistry and Ecotoxicology, Research Center for Eco-Environmental Sciences, Chinese Academy of Sciences, Beijing 100085, China. E-mail: hypeng@rcees.ac.cn*
[b] *College of Science, Northeastern University, Shenyang 110819, China*
[c] *University of Chinese Academy of Sciences, Beijing 100049, China*
† These authors contributed equally.

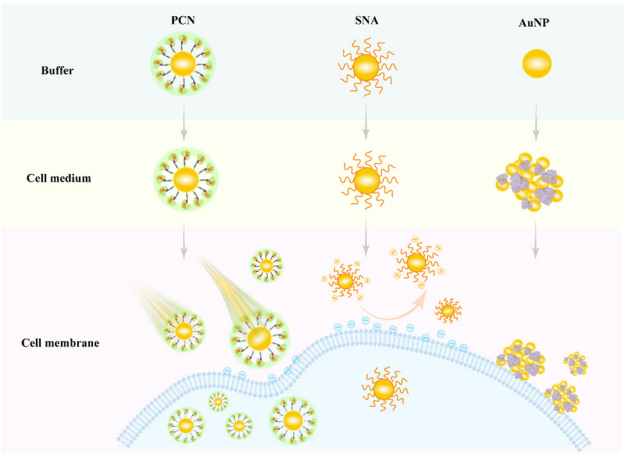


Scheme 1 Schematic diagram of the behavior of gold nanoparticles (AuNPs), spherical nucleic acids (SNAs) and protein corona nanostructures (PCNs) during incubation with cells.

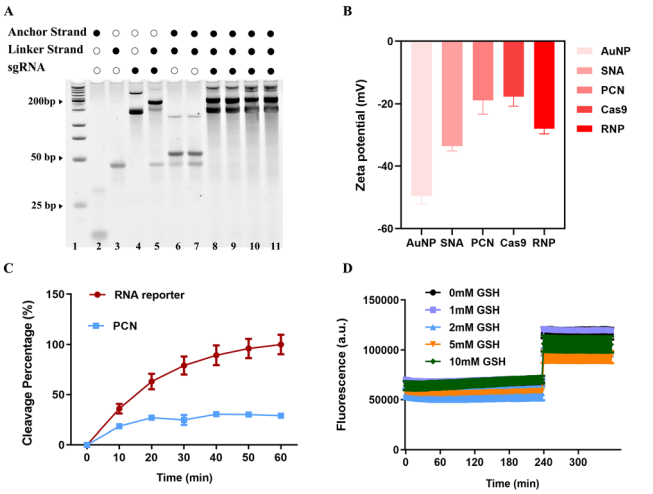


Fig. 1 Characterization and stability assessment of AuNPs, SNAs, and PCNs. (A) Polyacrylamide gel electrophoresis (PAGE) analysis of annealed products formed from an anchor, Cy5-linker, and sgRNA at varying molar ratios. Lanes: 1, marker; 2, anchor; 3, linker; 4, sgRNA; 5, sgRNA-Linker; 6–7, Anchor : linker (1 : 1.2, and 1 : 1.5); 8–11, anchor : linker : sgRNA (1 : 1.2 : 3, 1 : 1.5 : 3, 1 : 1.2 : 5, and 1 : 1.5 : 5). (B) Zeta potential measurements of AuNPs, SNA, PCN, free Cas9 protein, and RNP (Cas9–sgRNA complex). Stability comparison of PCN and control RNA reporters in 0.1% FBS (C), and under different concentrations of glutathione (GSH) (D).

crucial role in determining the spatial arrangement of the attached Cas9 protein, ensuring specific binding of the protein to the loop region of the extended sgRNA and the formation of a monolayer protein corona structure on the nanoparticle surface (Fig. S1).

Optimizing the annealing ratios of the nucleic acid strands on the gold nanoparticle surface was pivotal in achieving successful synthesis of the protein coronas. To enhance the attachment of the "anchor:linker:sgRNA" ternary complexes to the AuNPs, an excess of linker strands was essential to ensure complete pairing with all anchor strands, along with an excess of sgRNA to enable full hybridization with the anchor:linker duplex. By annealing the three strands in varying ratios, the optimal synthesis conditions were determined. Polyacrylamide gel electrophoresis (PAGE) analysis revealed that at an annealing ratio of anchor to linker of 1 : 1.2, complete hybridization occurred, leading to the disappearance of the anchor and linker bands. Similarly, at an annealing ratio of anchor : linker : sgRNA of 1 : 1.2 : 3, the desired three-strand complex band emerged, indicating successful synthesis, while excess sgRNA bands were also observed (Fig. 1A).

The average nucleic acid scaffold loading on the AuNPs was quantified using a fluorescence-based assay. Cy5-labeled linker strands were annealed with anchor and sgRNA at optimized ratios and anchored to AuNPs *via* Au–S bonds. Treatment with 2-mercaptoethanol disrupted the Au–S bonds, releasing the scaffolds and restoring Cy5 fluorescence. Comparing the fluorescence intensities before and after release with a Cy5-DNA standard curve (Fig. S2) revealed an average loading of ~54 scaffolds per AuNP. The quantification of the Cas9 protein using gel electrophoresis indicated a 64% Cas9 loading efficiency on the AuNPs at a 1 : 100 molar ratio of AuNP : Cas9 (Fig. S3).

Successful formation of the PCN was confirmed by characterization using UV-vis spectroscopy. It showed red-shifted absorption peaks for PCN by 5 nm *vs.* AuNPs and 3 nm *vs.* SNAs (Fig. S4A). DLS indicated a progressive increase in the hydrodynamic diameter from 32.7 nm (AuNP) to 105.7 nm (SNA) to 164.2 nm (PCN) (Fig. S4B). Zeta potential measurements further supported conjugation, increasing from citrate-stabilized AuNPs to SNAs, and increasing significantly for the PCN (Fig. 1B). Furthermore, the TEM results showed that the nucleic acid scaffolds and Cas9 have been successfully conjugated to the AuNPs, and the synthesized PCNs exhibit superior dispersion compared to AuNPs (Fig. S5).

The PCN significantly improved the AuNP stability in complex biological systems. In 0.1% FBS, an RNA reporter was degraded completely within 40 minutes, while RNA in PCN remained stable with less than 20% degradation (Fig. 1C). PCN also demonstrated prolonged stability against glutathione (GSH), and fluorescence restoration (indicating degradation/release) occurred only upon adding 2-mercaptoethanol (2-ME) to cleave Au–S bonds, not from GSH exposure alone (Fig. 1D).

PCN also conferred superior colloidal stability in serum-free culture medium. Unmodified AuNPs aggregated immediately (solution turned gray), while both SNA and PCN initially remained dispersed (light pink). After 16 hours, SNA-treated wells showed gray aggregates, whereas PCN maintained dispersion and retained a pink color (Fig. 2A), demonstrating essential stability for cellular delivery applications.

We then optimized the Cas9 to SNA incubation ratio to maximize cellular uptake efficiency. Cy5-labeled SNAs incubated with increasing Cas9 ratios formed PCNs with varying protein density (Fig. S6). Co-culture with HeLa-GFP cells showed that higher Cas9 ratios progressively increased the intracellular Cy5 signal (Fig. 2B), indicating enhanced transmembrane delivery. While all PCN ratios outperformed SNA, a Cas9 to SNA molar ratio of 100 : 1 was selected for subsequent studies to balance uptake efficiency with preventing aggregation.

While nonspecifically adsorbed proteins (*e.g.*, serum albumin) typically reduce nanoparticle–cell membrane interactions and hinder uptake efficiency,[18] our designed Cas9 protein

 

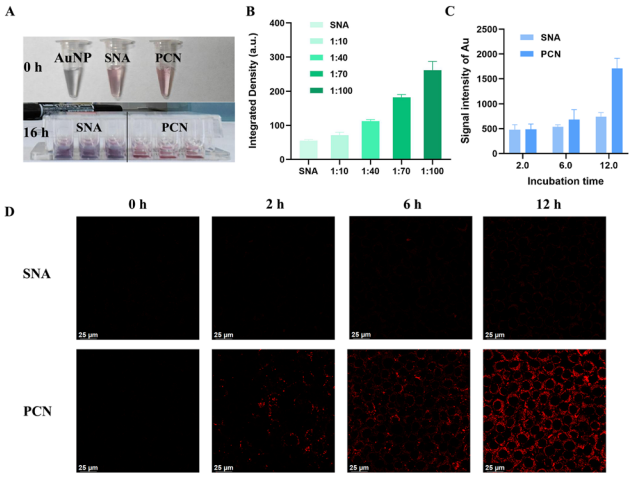


Fig. 2 Time-dependent cellular uptake of SNA and PCN in HeLa-GFP cells. (A) Visual assessment of colloidal stability in the cell medium: solution state immediately after adding 1 nM AuNPs, SNA, or PCN, and solution state after 16 h incubation in cell culture wells. (B) Quantitative analysis of intracellular Cy5 fluorescence intensity in HeLa-GFP cells after 6 h incubation with PCNs assembled at different SNA : Cas9 incubation ratios. (C) Intracellular Au concentration quantified by ICP-MS following incubation of HeLa-GFP cells with 1 nM SNA or PCN for 2, 6, and 12 h. Error bars represent ± 1 SD ($n$ = 3). (D) Confocal fluorescence images of HeLa-GFP cells incubated with Cy5-labeled SNA or PCN for 0, 2, 6, and 12 h (Cy5 signal: red). Scale bar: 25 μm.

corona nanostructure demonstrates an opposite effect. The Cas9 protein's positively charged residues neutralize the negatively charged nucleic acid-modified surface, while its functional nature may facilitate receptor targeting, both mechanisms promoting cellular internalization.[19,20] Furthermore, the monolayer corona's spatial arrangement potentially alters endocytic pathways,[21] collectively enhancing cellular uptake.

Quantitative ICP-MS analysis of intracellular Au concentration revealed time-dependent internalization differences between SNA and PCN (Fig. 2C). After 2 hours of incubation with HeLa-GFP cells, both systems showed comparable uptake. However, prolonged incubation (6–12 h) resulted in only marginal increases in SNA internalization, whereas PCN uptake surged significantly. By 12 hours, the intracellular Au concentration from PCN was 2.3-fold higher than that from SNA. Fluorescence imaging of Cy5-labeled constructs corroborated with the ICP-MS results (Fig. S7). SNA showed minimal signal increase over 12 h, while PCN exhibited a gradual, time-dependent increase in intracellular Cy5 signal (Fig. 2D), confirming sustained and enhanced PCN delivery.

We further investigated the uptake efficiency of PCN with increasing concentrations. Confocal imaging of HeLa-GFP cells incubated for 16 h with increasing concentrations (0.5–4 nM) of Cy5-labeled PCN showed progressively stronger intracellular Cy5 fluorescence (Fig. 3A and Fig. S8). Fluorescence colocalization analysis confirmed cytoplasmic localization: the Cy5 signal (PCN) overlapped extensively with the cytoplasmic FITC signal, but remained distinct from the nuclear DAPI staining (Fig. 3B). This demonstrates successful cytoplasmic internalization without nuclear entry.

ICP-MS quantification is aligned with the imaging results. The higher incubation concentrations increased intracellular Au for both SNA and PCN. Crucially, at 4 nM, PCN uptake was 4-fold greater than SNA (Fig. 3C). This significant enhancement, combined with the corona's excellent biocompatibility, suggests that the Cas9 protein corona actively promotes nanoparticle–membrane interactions,[22] surpassing the caveolin-mediated endocytosis typical of SNAs.[23]

We tracked the intracellular fate of the Cy5-labeled PCNs, specifically their interaction with lysosomes. Confocal fluorescence imaging after 2 hours of incubation revealed strong colocalization (Pearson's coefficient = 0.7) between the PCN (Cy5, red) and lysosomes (LysoTracker Yellow, green), indicating initial lysosomal capture (Fig. 4A). However, by 6 hours, the colocalization significantly diminished (Pearson's coefficient = 0.5), demonstrating that the PCNs gradually escape lysosomal entrapment and achieve cytoplasmic redistribution (Fig. 4B).

To further elucidate the cellular uptake mechanism of the PCN, we employed specific endocytosis inhibitors targeting distinct pathways: cytochalasin D (phagocytosis), chlorpromazine (clathrin-mediated), wortmannin (receptor-mediated), genistein, and methyl β-cyclodextrin (caveolae-mediated).[24] ICP-MS quantification of intracellular Au after 8 hours of incubation revealed significant pathway dependence. Chlorpromazine treatment severely impaired uptake, resulting in intracellular Au concentrations substantially lower than the inhibitor-free control. Uptake was also significantly reduced (~50% of control) by the caveolae inhibitors methyl β-cyclodextrin and genistein. In contrast, cytochalasin D and wortmannin had no significant effect on internalization efficiency (Fig. 4C). These results indicate that PCNs

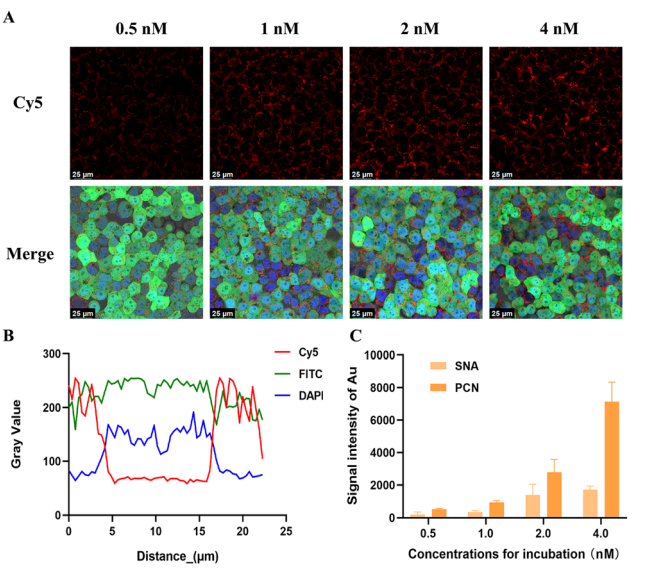


Fig. 3 Evaluation of SNA and PCN uptake in HeLa-GFP cells at varying concentrations. (A) Confocal images of PCN internalization (0.5–4 nM) (Cy5, red), cells (FITC, green), and nuclei (DAPI, blue). Scale bar: 25 μm. (B) Schematic of co-localization fluorescence analysis for a single representative HeLa-GFP cell. (C) ICP-MS measurement of intracellular Au after 16 h incubation with varying SNA and PCN concentrations. Error bars: ±1 SD ($n$ = 3).

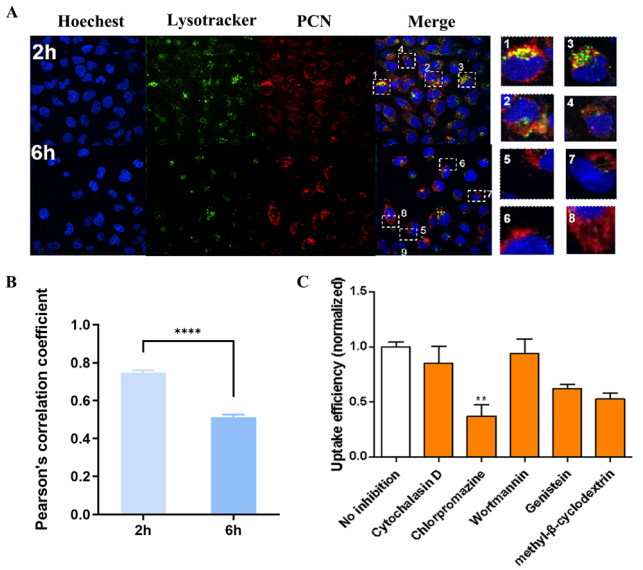


Fig. 4 Mechanism of PCN cellular uptake and lysosomal escape. (A) Representative confocal images showing PCN localization relative to lysosomes and nuclei: DAPI (blue, nuclei), Cy5 (red, PCN), LysoTracker Yellow HCK-123 (green, lysosomes). (B) Lysosome-PCN co-localization analysis: Pearson correlation coefficient values at 2 h and 6 h incubation. (C) Effect of endocytosis inhibitors on PCN internalization efficiency, measured *via* ICP-MS.

primarily enter cells *via* clathrin-mediated endocytosis, with caveolae-mediated endocytosis playing a substantial auxiliary role.

In summary, we successfully engineered uniform monolayer protein corona around AuNPs through nucleic acid–protein assembly. This strategy achieves precise spatial arrangement of proteins on the nanoparticle surface, significantly enhancing both cellular uptake efficiency and biological stability while preserving the inherent optical properties and nanoscale functionality of the gold core. These advances substantially expand the biomedical utility of PCNs for applications including drug delivery, photothermal therapy, contrast imaging, and biosensing.[25–29] Future exploration will focus on exploiting the Cas9–sgRNA complex for targeted gene editing delivery and extending this versatile platform to incorporate diverse nucleic acid aptamer-functional protein pairs, broadening its combinatorial potential and therapeutic scope.

H. P. acknowledges the financial support from the National Key Research and Development Program of China (2023YFA0915102), the Strategic Priority Research Program of the Chinese Academy of Sciences (XDB0750100) and the National Natural Science Foundation of China (grant no. 22276199). R. S. thanks the Youth Fund from the National Natural Science Foundation of China (grant no. 22206201) for the financial support.

## Conflicts of interest

There are no conflicts to declare.

## Data availability

The data supporting this article have been included in the SI. See DOI: https://doi.org/10.1039/d5cc03658e

## Notes and references

1 L. Dykman and N. Khlebtsov, *Chem. Soc. Rev.*, 2012, **41**, 2256–2282.
2 A. Albanese, P. S. Tang and W. C. W. Chan, *Annu. Rev. Biomed. Eng.*, 2012, **14**, 1–16.
3 Y. Pan, S. Neuss, A. Leifert, M. Fischler, F. Wen, U. Simon, G. Schmid, W. Brandau and W. Jahnen-Dechent, *Small*, 2007, **3**, 1941–1949.
4 Z. Ye, W. Liao, Z. Deng, L. Wang, B. Wen, D. Zhang, H. Wang, W. Xie and H. Peng, *TrAC, Trends Anal. Chem.*, 2024, 175.
5 D. R. Bhumkar, H. M. Joshi, M. Sastry and V. B. Pokharkar, *Pharm. Res.*, 2007, **24**, 1415–1426.
6 M. Tebbe, C. Kuttner, M. Maennel, A. Fery and M. Chanana, *ACS Appl. Mater. Interfaces*, 2015, **7**, 5984–5991.
7 A. Anaki, C. Tzror-Azankot, M. Motiei, T. Sadan and R. Popovtzer, *Nanoscale Adv.*, 2024, **6**, 5420–5429.
8 C. H. J. Choi, C. A. Alabi, P. Webster and M. E. Davis, *Proc. Natl. Acad. Sci. U. S. A.*, 2010, **107**, 1235–1240.
9 T. Y. Chen, M. R. Chen, S. W. Liu, J. Y. Lin, Y. T. Yang, H. Y. Huang, J. K. Chen, C. S. Yang and K. M. C. Lin, *Int. J. Mol. Sci.*, 2020, **21**, 8158.
10 K. Knop, R. Hoogenboom, D. Fischer and U. S. Schubert, *Angew. Chem., Int. Ed.*, 2010, **49**, 6288–6308.
11 T. Cedervall, I. Lynch, S. Lindman, T. Berggard, E. Thulin, H. Nilsson, K. A. Dawson and S. Linse, *Proc. Natl. Acad. Sci. U. S. A.*, 2007, **104**, 2050–2055.
12 C. D. Walkey, J. B. Olsen, H. Guo, A. Emili and W. C. W. Chan, *J. Am. Chem. Soc.*, 2012, **134**, 2139–2147.
13 M. P. Monopoli, D. Walczyk, A. Campbell, G. Elia, I. Lynch, F. B. Bombelli and K. A. Dawson, *J. Am. Chem. Soc.*, 2011, **133**, 2525–2534.
14 M. Barz, W. J. Parak and R. Zentel, *Adv. Sci.*, 2024, **11**, 2198–3844.
15 J. C. Y. Kah, J. Chen, A. Zubieta and K. Hamad-Schifferli, *ACS Nano*, 2012, **6**, 6730–6740.
16 T. Zhao, M. Ren, J. Shi, H. Wang, J. Bai, W. Du and B. Xiang, *Biomed. Pharmacother.*, 2024, 175.
17 H. Nishimasu, F. A. Ran, P. D. Hsu, S. Konermann, S. I. Shehata, N. Dohmae, R. Ishitani, F. Zhang and O. Nureki, *Cell*, 2014, **156**, 935–949.
18 W. Kim, N. K. Ly, Y. He, Y. Li, Z. Yuan and Y. Yeo, *Adv. Drug Delivery Rev.*, 2023, **192**, 1872–8294.
19 R. Cai and C. Chen, *Adv. Mater.*, 2019, **31**, 1521–4095.
20 M. Barbalinardo, F. Caicci, M. Cavallini and D. Gentili, *Small*, 2018, **14**, 1613–6829.
21 X. Cheng, X. Tian, A. Wu, J. Li, J. Tian, Y. Chong, Z. Chai, Y. Zhao, C. Chen and C. Ge, *ACS Appl. Mater. Interfaces*, 2015, **7**, 20568–20575.
22 J. Wu, H. Peng, X. Lu, M. Lai, H. Zhang and X. C. Le, *Angew. Chem., Int. Ed.*, 2021, **60**, 11104–11109.
23 A. Mokhtarzadeh, H. Vahidnezhad, L. Youssefian, J. Mosafer, B. Baradaran and J. Uitto, *Trends Mol. Med.*, 2019, **25**, 1066–1079.
24 V. Francia, K. Yang, S. Deville, C. Reker-Smit, I. Nelissen and A. Salvati, *ACS Nano*, 2019, **13**, 11107–11121.
25 A. Yuan, T. Sun, L. Chen, D. Zhang, W. Xie and H. Peng, *Anal. Chem.*, 2024, **96**, 20074–20081.
26 A. Yuan, R. Sha, W. Xie, G. Qu, H. Zhang, H. Wang, X. C. Le, G. Jiang and H. Peng, *J. Am. Chem. Soc.*, 2024, **146**, 26657–26666.
27 R. Sha, H. Qin, A. Yuan, Z. Deng, W. Liao, G. Qu, B. Wen, W. Xie and H. Peng, *Chem. – Asian J.*, 2025, 1861–4728.
28 Q. Liu, Y. Ouyang, Y. Wang, S. Zhou, Y. Zhan and L. Wang, *Adv. Healthcare Mater.*, 2025, 2405058.
29 L. Wang, S. Zhou, Y. Wang, Y. Wang, J. Li, X. Chen, D. Zhou, L. Liang, B. Yin, Y. Zhang and L. Wang, *Faraday Discuss.*, 2025, **257**, 60–72.